

Article

A Revised Temporal Scaling Method to Yield Better ET Estimates at a Regional Scale

Yi Song ^{1,*}, Mingguo Ma ², Long Jin ³ and Xufeng Wang ⁴

¹ State Key Laboratory of Loess and Quaternary Geology, Institute of Earth Environment, Chinese Academy of Sciences, Xi'an 710075, China

² School of Geographical Sciences, Southwest University, Chongqing 400715, China; E-Mail: mmg@swu.edu.cn

³ Key Laboratory of Highway Construction & Maintenance Technology in Permafrost Regions, Ministry of Transport, CCCC First Highway Consultants Co., LTD, Xi'an 710065, China; E-Mail: jlcoolmail@163.com

⁴ Cold and Arid Regions Environmental and Engineering Research Institute, Chinese Academy of Sciences, Lanzhou 730000, China; E-Mail: wangxufeng@lzb.ac.cn

* Author to whom correspondence should be addressed; E-Mail: songyi@ieecas.cn; Tel.: +86-29-6233-6290.

Academic Editors: Yuei-An Liou, Qinhua Liu, Xin Li, George P. Petropoulos and Prasad S. Thenkabail

Received: 18 December 2014 / Accepted: 15 May 2015 / Published: 21 May 2015

Abstract: This study presents a revised temporal scaling method based on a detection algorithm for the temporal stability of the evaporative fraction (EF) to estimate total daytime evapotranspiration (ET) at a regional scale. The study area is located in the Heihe River Basin, which is the second largest inland river basin in China. The remote sensing data and field observations used in this study were obtained from the Heihe Watershed Allied Telemetry Experimental Research (HiWATER) project. The half-hourly EF values (EF^{EC}) calculated using meteorological observations from an eddy covariance (EC) system and an automatic meteorological station (AMS) represented the diurnal pattern of the EF across the majority of the study area. The remotely sensed instantaneous midday EF (EF^{ASTER}), which indicates the spatial distribution of the midday EF over the entire study area, was calculated from an Advanced Spaceborne Thermal Emission and Reflection Radiometer (ASTER) image. The temporal stability of EF^{EC} was examined using a detection algorithm. Intervals with inconsistent EF^{EC} values were distinguished from those

with consistent EF^{EC} values; the total daytime ET (from 9:00 to 19:00) within these interval types was integrated separately. Validation of the total daytime ET at the satellite pixel scale was conducted using measurements from 17 EC towers. Using the detection algorithm for the temporal stability of the EF and dynamic adjustment, the revised temporal scaling method resulted in a root-mean-square error (RMSE) of 0.54 ($\text{mm}\cdot\text{d}^{-1}$), a mean relative error (MRE) of 7.26% and a correlation coefficient (Corr.) of 0.81; all of these values were superior to those of the two other methods (*i.e.*, the constant EF and variable EF methods). The revised method easily extends to other areas and exhibits a superior performance in flat and regularly-irrigated farmlands at the regional scale.

Keywords: arid irrigated farmlands; evapotranspiration; temporal scaling; evaporative fraction; regional scale

1. Introduction

Evapotranspiration (ET) plays an important role in hydrology, meteorology and agriculture by controlling the water cycle and energy transport within the biosphere, atmosphere and hydrosphere [1–3]. Because the hydrological cycle is strongly affected by crop water consumption in semiarid agricultural regions, precise ET estimates are important for saving water through efficient irrigation practices [4,5]. Remotely sensed data can provide instantaneous two-dimensional spatial information on ground surface properties, such as albedo, vegetation fraction, land surface temperature and net radiation (R_n). These properties are important variables for remotely sensed ET estimates [6–8]. However, in many ET-related disciplines, total daily, weekly and monthly ET readings, rather than instantaneous values, are required at multiple scales. Therefore, to convert instantaneous spatial ET values to time-integrated values, temporal scaling is required. Current ET estimation models, such as the surface energy balance system (SEBS) [9], the surface energy balance algorithm for land (SEBAL) [10], and two-source models for evapotranspiration, such as TTME [11] and TSEBPS [12], primarily depend on observations during satellite overpasses. Several studies have been conducted to convert the instantaneous latent heat flux (λE) to the integrated ET, either using a numerical model that simulates the diurnal surface temperature under realistic conditions or using assumptions about the relationship between instantaneous ET and daily values [3]. Sine function [13] and constant evaporative fraction (EF) [14] methods are commonly used for scaling instantaneous λE to total integrated ET [3,15]. Jackson *et al.* [13] used a sine function to relate the ratio of instantaneous ET to daily ET to the diurnal trend of solar irradiance. Sugita and Brutsaert [14] proposed the constant EF method, which assumes that the EF is sufficiently constant during the daytime, to determine the regional daily ET. The sine function provides a good approximation of the change in diurnal solar irradiation from approximately sunrise to sunset on sunny days. However, this method has limited accuracy on cloudy days due to its empirical nature [15]. The variability or conservation of the EF on a given individual day was affected by complicated combinations of factors, including weather conditions, soil moisture, topography, biophysical conditions, cloudiness and the advection of moisture and heat [16]. Allen *et al.* [16] proposed a constant reference EF method to capture the impacts of advection and changing wind and

humidity conditions in ET temporal scaling. Because it considers orographic effects, this method is more applicable over terrain areas. Tomás *et al.* [17] used a triangle method to estimate instantaneous EF during satellite overpass times over large semi-arid areas with uniform landscapes. Several studies based on *in situ* measurements and analyses that consist of land surface process modeling have indicated that the EF curve is concave upward and is relatively stable during the daytime under dry conditions [18–22]. Suleiman and Crago reported that the EF increases with the amount of vegetation, soil moisture, and air dryness [23]. Hoedjes *et al.* [19] showed that the EF curve is markedly concave upward under wet conditions and developed a new heuristic parameterization based on routine daily meteorological observations and remotely sensed estimates of instantaneous EF to consider the dependence on soil and vegetation conditions. However, the EF values in the afternoon are unstable relative to those in the morning [22]. The variable EF method [19] better approximates the true EF values under wet conditions in the morning, although the study did not address the large fluctuations in the afternoon.

We studied the Zhangye Oasis of the Heihe River Basin, which is the second largest inland river basin in the arid region of Northwest China [24]. The main land use type in our study area is a typical irrigated farmland. The primary crop is seed corn. According to Yang [25], who conducted a study in the same area, the assumption that EF can be treated as constant during the daytime (so-called EF self-preservation) no longer holds over corn growing seasons because the ET diurnal pattern is primarily influenced by stomatal regulation. The constant EF method and the variable EF method have particular limitations in irrigated farmlands of arid regions because of the special land cover and climate conditions. A detection algorithm conducted in this revised ET temporal scaling method was applied to examine the temporal stability of the EF values, which were calculated from eddy covariance (EC) and automatic meteorological station (AMS) measurements. The primary objectives of this study were (1) to consider the temporal and spatial heterogeneity of the EF in the temporal scaling method; (2) to compare the results estimated using the revised method with those estimated using the other two temporal scaling methods (*i.e.*, the constant EF method and the variable EF method); (3) to assess the applicability of the revised method to farmlands in arid regions; and (4) to obtain better regional ET products.

2. Data

The field observations and remote sensing images used in this study were derived from the Heihe Watershed Allied Telemetry Experimental Research (HiWATER) project. HiWATER is a comprehensive eco-hydrological experiment under the framework of the Heihe Plan and is based on the diverse needs of interdisciplinary research and existing observational infrastructures in the basin [26]. The intensive observation period of the fieldwork began in May 2012 in the middle reaches of the river.

2.1. Field Observations

Within the Yingke and Daman irrigation districts of the Zhangye Oasis, an observation matrix that consists of 17 stations was built. Each station was equipped with an EC tower and an AMS. The land surface of the observation area is heterogeneous and is dominated by seed corn, corn planted with spring wheat, vegetables, orchards and residential areas (see Figure 1). The observations used in this

study include humidity (sensor type: Avalon AV-14TH), 4 radiation components (total solar radiation, reflective shortwave radiation, land surface long wave radiation, and atmospheric long wave radiation; sensor type: Kipp & Zonen CNR 4, Eppley PIR & PSP), land surface temperature (sensor type: Avalon IRTC3), soil temperature (sensor type: Avalon AV-10T) and moisture (sensor type: Campbell CS616) profiles and turbulent fluxes (sensor type: CSAT3 + LI7500A) [27].

The raw high-frequency (10-Hz) data collected at the EC towers were successively processed through de-spiking [28], tilt correction [29], sonic virtual temperature corrections [30], time-lag calculations, frequency response corrections [31] and Webb, Pearman and Leuning (WPL) correlations [32]. These processes were completed using the EdiRe software developed by Edinburgh University, UK. The half-hour-averaged λE and sensible heat flux (H) values were calculated from the post-processed EC data [33]. The records with a friction velocity of less than $0.1 \text{ (m}\cdot\text{s}^{-1}\text{)}$ were not used in the energy balance closure analysis or ET validation. The energy balance closure from 1 July to 15 August reached 90%.

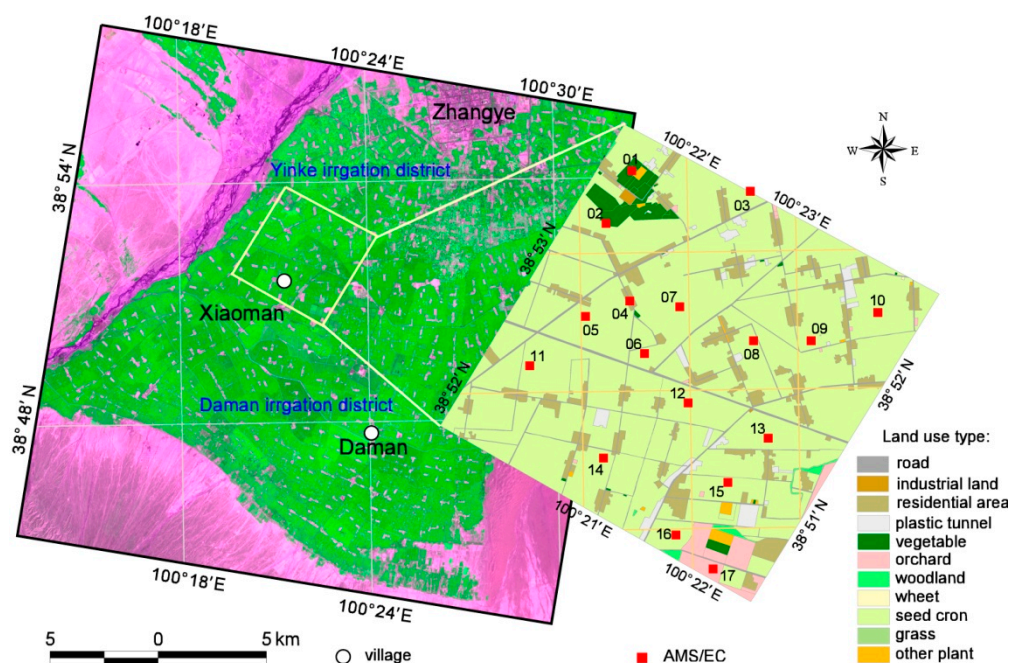


Figure 1. Land cover and the meteorological instrumentation configuration in the study area.

2.2. Satellite Images

Meteorological data from the HiWATER middle reaches experiment had the highest integrity from June to August 2012. To maintain the soil moisture, seedlings were covered with plastic film. This plastic film can introduce uncertainty into the ET observations by blocking a portion of the vapor, which is not observable by the EC systems. After July, the corn grew up, the plastic film was broken, and the field ridges were closely spaced. The remaining plastic film residue in the soil did not have a large impact on the ET observations. Thus, the images used in our study were selected from July to August. During this period, three Advanced Spaceborne Thermal Emission and Reflection Radiometer (ASTER) L1B images acquired on 10 July, 2 August and 11 August of 2012 were used for estimating the ET from remote sensing data. The images were pre-processed through radiative, atmospheric and

geometric corrections with Environment for Visualizing Images (ENVI). Atmospheric correction was conducted using ENVI Fast Line-of-sight Atmospheric Analysis of Hypercubes (FLAASH). First, the processed images were used to estimate instantaneous ground surface properties, including albedo, emissivity and vegetation fraction, at ASTER overpasses. Next, instantaneous surface heat fluxes, including λE , ground heat flux (G) and available energy (A), were estimated based on the ground surface properties. Then, the instantaneous EF and Bowen ratio during ASTER overpass times were calculated. The specific calculations are introduced in Section 3.4.

3. Methods

3.1. Constant EF Method (cEF)

The cEF method assumes that the daily EF remains relatively constant despite particular daily variations. This ‘self-preservation’ of the EF has allowed for the use of midday EF values for converting instantaneous remotely sensed λE to total daily values [18,19,34]. From ASTER L1B images, the instantaneous midday EF (EF_{ASTER}) was estimated during ASTER overpass times as follows:

$$EF_{ASTER} = \lambda E_{ASTER} / (R_{nASTER} - G_{ASTER}) \quad (1)$$

Then, the EF_{ASTER} values were multiplied by the total daytime R_n (from 9:00 to 19:00) minus the total daytime G (from 9:00 to 19:00) to estimate the total daytime ET (from 9:00 to 19:00). Remotely sensed λE_{ASTER} values were estimated using a revised surface resistance model [35]. G_{ASTER} values were estimated using the same parameterization proposed in SEBS [9]. Other remotely sensed land surface variables and half-hourly R_{ni} and G_i were the same in the three methods. The specific calculations are introduced in Section 3.4.

3.2. Variable EF Method (vEF)

The ‘self-preservation’ assumption of the EF is not valid under wet conditions [18,19]. During the daytime, the EF of bare soil is more stable than that of regularly-irrigated farmlands whose EF curve is concave upward. To distinguish farmlands under wet conditions from bare soil under dry conditions, Hoedjes *et al.* [19] used a dynamic coefficient to adjust the EF values, which better approximate the true value under wet conditions in the morning [15]. The adjustment factor (r) can be defined as follows:

$$r_i = EF_i^{sim} / EF_{11:30}^{sim} \quad (2)$$

where EF_i^{sim} is the simulated EF of the i^{th} time step (half hour), which is a function of the incoming solar radiation (S_i^\downarrow , $W \cdot m^{-2}$) and the relative humidity (RH , %):

$$EF_i^{sim} = 1.2 - (0.4 \times S_i^\downarrow / 1000 + 0.5 \times RH_i / 100) \quad (3)$$

and $EF_{11:30}^{sim}$ is the simulated EF during the ASTER overpass (11:30 UTC).

The Bowen ratio during an ASTER overpass (β_{ASTER}) was estimated as follows:

$$\beta_{ASTER} = (R_{nASTER} - G_{ASTER} - \lambda E_{ASTER}) / \lambda E_{ASTER} \quad (4)$$

Under dry conditions, β_{ASTER} exceeds 1.5; thus, EF_{ASTER} was used for temporal scaling. When β_{ASTER}

did not exceed 1.5, EF_{ASTER} was optimized by the r_i value of the corresponding time step:

$$EF_i^{opt} = EF_{ASTER} \times r_i. \quad (5)$$

3.3. Revised Variable EF Method (vEFr)

The adjusted EF curve, which was simulated using the vEF method, displayed a concave upward shape that better approximates the true value under wet conditions in the morning. However, the EF values in the afternoon (after 14:00) are unstable relative to those in the morning [22]. The vEF method does not address the large afternoon fluctuations. To address the high temporal heterogeneity of the EF in the afternoon under wet conditions, a detection algorithm for the temporal stability of the EF was conducted in the revised temporal scaling method for irrigated fields. The half-hourly EF (EF^{EC}) values calculated from the meteorological observations from tower AMS/EC12 were used as references to represent the EF diurnal pattern across most of the study area:

$$EF_i^{EC} = \lambda E_i / A_i, \quad (6)$$

where the subscript i is the EF time step (half hour), and A is the available energy, which is equal to the R_n observed by the net radiometer on tower AMS12 minus G . In addition, the half-hourly λE_i values were obtained from tower EC12. The half-hourly G_i values were calculated using soil moisture and temperature profiles observed by tower AMS12 based on a temperature prediction—correction method suggested by Yang and Wang [36]. The logic behind the detection algorithm for determining the temporal stability of the EF is shown in Figure 2. The detection algorithm used a moving window to search for a continuous time interval with relatively stable EF^{EC} values. When the absolute value of the difference between EF_i^{EC} and the mean value of the stable EF^{EC} values was lower than a particular threshold, EF_i^{EC} was considered relatively stable. However, determining the mean value of the stable EF^{EC} values and the threshold was problematic. The atmosphere is generally more stable in the morning than in the afternoon. Thus, the EF values in the morning (from approximately 9:00 to 12:00) are steady relative to those in the afternoon [22]. A moving window (2.5 h) was used to scan the EF^{EC} values from 9:00 to 14:00. The mean values (u) of the EF^{EC} and their standard deviations (σ) within each window were calculated. The window with the minimum σ (σ_{min}) was considered as a continuous time interval with less unstable EF values. The mean value for the window with the minimum σ ($u_{\sigma_{min}}$) was considered as the mean of the stable EF^{EC} values, and the σ_{min} provided the threshold. Then, the moving window scanned all EF^{EC} values from 9:00 to 19:00 to identify the stable EF^{EC} . Each EF_i^{EC} was classified as stable if $|EF_i^{EC} - u_{\sigma_{min}}| \leq \sigma_{min}$.

Therefore, the total daytime ET (from 9:00 to 19:00) was calculated as follows:

$$ET_{dt} = \sum_9^{19} [(A_i \cdot EF_i \cdot t) / (L \cdot \rho_w) \times 10^3], \quad (7)$$

where t represents a half hour (in seconds); L is the latent heat of vaporization ($2.45 \times 10^6 \text{ J} \cdot \text{kg}^{-1}$); and ρ_w is the density of water ($1000 \text{ kg} \cdot \text{m}^{-3}$). Within the interval that EF^{EC} remains stable, the midday EF_{ASTER} was optimized via r in Equation (5) under wet conditions (β_{ASTER} below 1.5) while keeping the original value under dry conditions (β_{ASTER} exceeding 1.5). When EF_i^{EC} exhibited large variations,

EF_{ASTER} was replaced by EF_t^{EC} in the corresponding time step during the temporal scaling process. Although EF^{EC} values are point measurements that ignore the spatial heterogeneity of the EF, the error induced by replacing EF_{ASTER} with EF_t^{EC} should be smaller than that produce by ignoring the temporal heterogeneity for conditions in which EF greatly fluctuates. This point is discussed in Section 5.2. The input data required in these three methods are shown in Table 1, and the logic behind the vEFr method is shown in Figure 3.

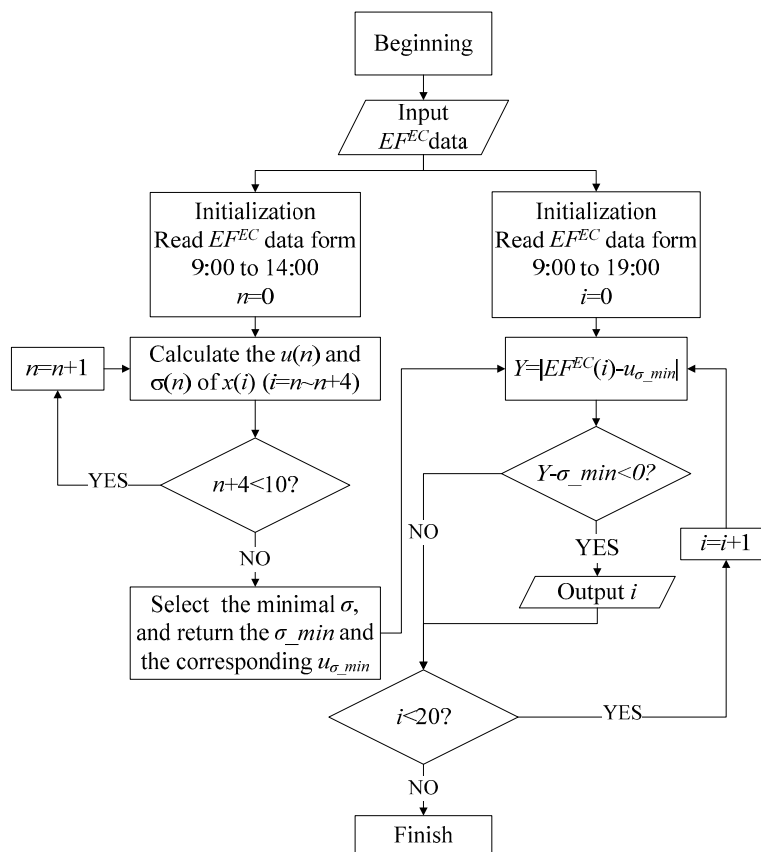


Figure 2. Flowchart of the detection algorithm.

Table 1. Input for the three methods.

Methods	Spatial Input	Common Input
cEF	None	Midday constant EF_{ASTER} Half-hourly total solar radiation and half-hourly atmospheric long wave radiation Remotely sensed land surface emissivity Remotely sensed surface albedo Remotely sensed f_c
vEF	Remotely sensed β_{ASTER} Adjustment factor calculated from meteorological observations	
vEFr	Remotely sensed β_{ASTER} Adjustment factor calculated from meteorological observations Half-hourly EF^{EC} values	

Note: The remotely sensed EF_{ASTER} , β_{ASTER} , land surface emissivity, albedo and f_c used in the three temporal scaling methods were estimated from ASTER L1B images. The time period for the total solar radiation, atmospheric long wave radiation, adjustment factor, and EF^{EC} is 9:00 to 19:00.

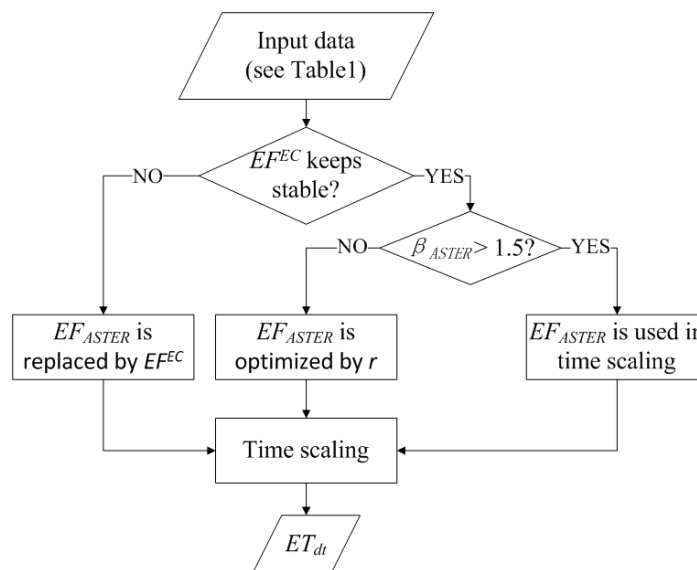


Figure 3. Flowchart of the revised temporal scaling method.

A validation of the land surface ET at the satellite pixel scale was conducted using measurements collected from 17 EC systems. An innovative validation method for remotely sensed ET using EC measurements [37] was used in our study. The observations from the EC system represent a weighted average over a range that primarily contributes to the measurement, namely the source area, which depends on the measurement height, wind direction/velocity, atmospheric stability and the underlying surface conditions. It has been suggested that all pixels within the EC system source area should be considered as validation pixels [35,37]. By determining the footprint based on the model of Kormann and Meixner [38], the source area and the footprint-relative weights (relative contribution) during the passage times of the three images can be acquired. The remotely sensed ET estimates were overlapped using the relative contribution of EC systems. The weighted average remotely sensed ET ($ET_{weighted}$) was computed as follows:

$$ET_{weighted} = \sum_{p=1}^n (w_p \times ET_p), \tag{8}$$

where n is the number of pixels within the source area; w_p and ET_p are the relative weight and ET estimate, respectively, of each pixel within the source area.

3.4. Remotely Sensed Estimation for Land Surface Variables

The land surface variables of albedo and emissivity cannot be obtained at times other than during the ASTER overpass. Thus, the albedo and emissivity are assumed to be constant during the daytime. The assumption that the albedo is constant throughout the day may be unrealistic [39]. However, this assumption is not critical for accurately retrieving the available energy [19]. The surface albedo (α) was estimated from the reflectance in bands 1, 3, 5, 6, 8 and 9 of the ASTER L1B images [40] using

$$\alpha = 0.484 \times R_1 + 0.335 \times R_3 - 0.324 \times R_5 + 0.551 \times R_6 + 0.305 \times R_8 - 0.367 \times R_9 - 0.0015 \tag{9}$$

The land surface emissivity was calculated using the normalized difference vegetation index (NDVI) threshold method [41,42] as follows:

$$\varepsilon = f_c R_v \varepsilon_v + (1 - f_c) R_s \varepsilon_s + d\varepsilon, \quad (10)$$

Where ε_v and ε_s are the emissivity of the full canopy (0.986) and bare soil (0.97215), respectively [42]; R_v and R_s are the temperature ratios of the full canopy and bare soil, respectively, which are estimated according to the fractional canopy coverage (f_c) [42]:

$$R_v = 0.9332 + 0.0585f_c, \quad R_s = 0.9902 + 0.1068f_c, \quad (11)$$

and $d\varepsilon$ is estimated as follows [41]:

$$d\varepsilon = \begin{cases} 0.003796f_c & f_c \leq 0.5 \\ 0.003796(1 - f_c) & f_c > 0.5 \end{cases} \quad (12)$$

Here, f_c is calculated using the NDVI [43]:

$$f_c = \left[\frac{NDVI - NDVI_{min}}{NDVI_{max} - NDVI_{min}} \right]^2, \quad (13)$$

where $NDVI_{max}$ and $NDVI_{min}$ are 0.7 and 0.05, respectively.

The land surface temperature (LST) in the i^{th} time step for one pixel is composed of the surface temperatures of the bare soil (T_s) and full canopies (T_v) in the same time step [44]. These two limiting cases were spatially interpolated using f_c :

$$LST_i = f_c T_{vi} + (1 - f_c) T_{si}, \quad (14)$$

where the subscript i represents the i^{th} time step (half hour).

According to the principles of microclimatology, the LST varies sinusoidally during the day. The T_s and T_v curves were observed by infrared radiometers installed on the AMS towers located in bare soil and full canopies (see Figure 4). The surface temperatures of the canopy and bare soil in the i^{th} time step were simulated as follows:

$$T_{vi} = \bar{T}_v + a_v \sin\left(2\pi t^* / \omega - \varphi\right), \quad (15)$$

$$T_{si} = \bar{T}_s + a_s \sin\left(2\pi t^* / \omega - \varphi\right), \quad (16)$$

where \bar{T}_v and a_v are the mean and amplitude of the surface temperature curves of the canopy, respectively; \bar{T}_s and a_s are the mean and amplitude of the surface temperature curves of the bare soil, respectively; t^* is the time (in hours on a 24-hour basis) after sunrise; and ω is the cycle of the surface temperature curves (which should be equivalent to 24 h). However, a half cycle is less than 12 h because the overnight land surface temperature does not have a sinusoidal curve. In addition, the T_v and T_s estimates match the observations during the daytime better when the half cycle is set to 10 h. φ is the initial phase of the temperature curve and is related to the local latitude (l) and the solar declination (sd), which is defined as follow:

$$\varphi = \left[\cos(-\tan(l) \times \tan(sd)) \right]^{-1}. \quad (17)$$

Tower AMS/EC04 was placed on a bare field next to a settlement, and tower AMS/EC12 was placed on farmland with densely planted seed corn. The T_v and T_s curves were fitted using the observations of infrared radiometers installed on towers AMS04 and AMS12, respectively. The parameters and root-mean-square error (RMSE) of the T_v and T_s estimates are shown in Table 2.

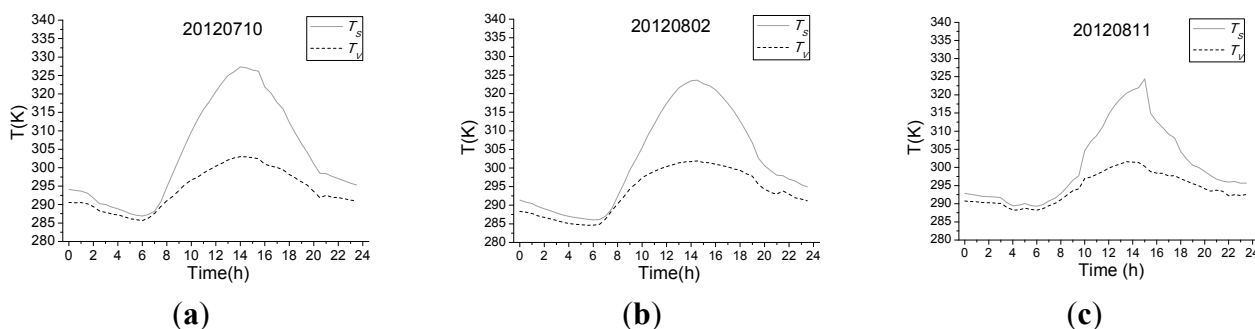


Figure 4. The T_s (observed by tower AMS04) and T_v (observed by tower AMS12) curves on (a) 10 July, (b) 2 August and (c) 11 August of 2012.

Table 2. Regression parameters of the T_s and T_v curves and the root-mean-square errors (RMSEs).

Date (yyyy/mm/dd)	\bar{T}_s (K)	a_s (K)	RMSE (K)	\bar{T}_v (K)	a_v (K)	RMSE (K)
20120710	300.48	26.67	1.87	296.88	4.81	1.12
20120802	300.62	23.90	1.37	293.60	8.94	1.45
20120811	300.91	15.44	3.64	294.14	6.50	1.52

Half-hourly R_{ni} values were calculated using instantaneously remotely sensed α and ε , half-hourly LST_i values that were spatially interpolated using f_c and half-hourly observations of total solar radiation (R_{Si}) and atmospheric long wave radiation (R_{Li}):

$$R_{ni} = (1 - \alpha)R_{Si}^{\downarrow} + \varepsilon R_{Li}^{\downarrow} - \varepsilon \sigma LST_i^4 \quad (18)$$

Then, half-hourly G_i values were estimated using the same parameterization proposed in SEBS [9]:

$$G_i = R_{ni} \times [\Gamma_c + (1 - f_c) \times (\Gamma_s - \Gamma_c)] \quad (19)$$

The ratios between the soil heat flux and the net radiation for the full vegetation canopy (Γ_c) and bare soil (Γ_s) were 0.05 [45] and 0.315 [46], respectively.

4. Results and Validation

According to the results of the detection algorithm for the temporal stability of the EF, the EF^{EC} values remained stable over particular daytime intervals and fluctuated before sunset and after sunrise (see Table 3).

Table 3. Stability of EF^{EC} on 10 July, 2 August, and 11 August of 2012.

Date (yyyy/mm/dd)	Stable Time (In Hours on A 24-Hour Basis)
20120710	11–16, 17.5
20120802	9–16, 17.5
20120811	9, 10–14.5

The EF values (see Figure 5) remained relatively stable from 10:00 to 15:00 with some variability during the early morning and late afternoon based on the surface and atmospheric conditions. The soil moisture on 10 July was higher than that on the other two days because most of the fields had recently been irrigated. Compared with the other two days, the EF on 10 July was less stable. However, the soil

moisture on 11 August was the lowest of the three days. Only the field near tower EC14 had been irrigated after 31 July. Thus, the EF from tower EC14 was higher than that from the other stations. The solid azure line in Figure 5 shows the optimized EF values calculated using the vEF method. The optimized EF values were approximately the true values for the corresponding EF^{EC} values in the morning. However, the vEF method did not simulate the significant increase in the EF after 15:00.

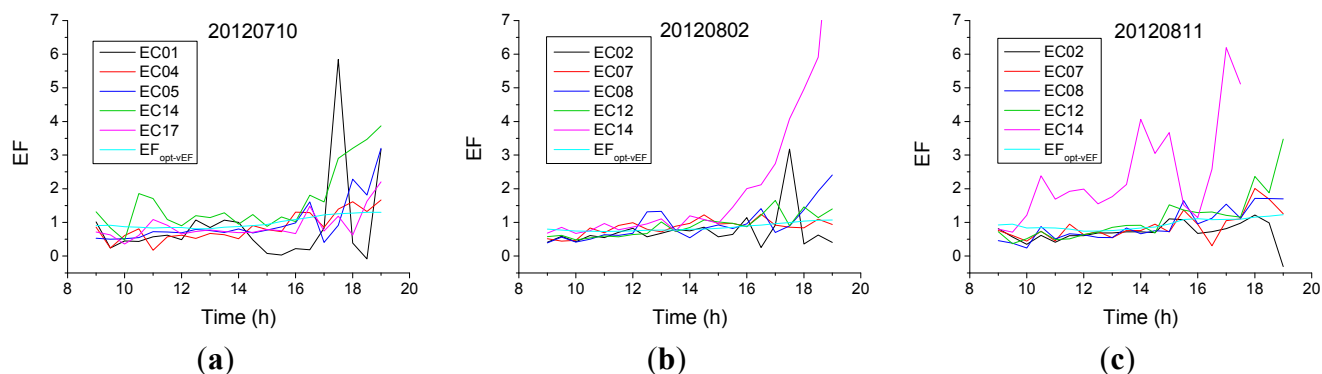


Figure 5. The EF values calculated from EC and AMS observations on (a) 10 July, (b) 2 August, and (c) 11 August of 2012. Note: the EF values in azure were optimized using the vEF method for EC05 on 10th July and EC08 on the other two days.

Among these three ET temporal scaling methods, the cEF method resulted in the lowest ET estimates (see Figure 6). The mean ET values from the cEF method on 10 July, 2 August and 11 August of 2012 were 4.89, 4.01 and 2.89 ($\text{mm}\cdot\text{d}^{-1}$), respectively. The transpiration on 11 August was the lowest of the three days because the corn tassels had been cut off. The distributions of the three ET results were similar. Villages, areas with regular shapes, roads, and straight lines in the figures displayed low ET values.

From the validation results (see Tables 4–6), the estimates from the vEFr method with a RMSE of ($0.54 \text{ mm}\cdot\text{d}^{-1}$), a mean relative error (MRE) of 7.26% and a correlation coefficient (Corr.) of 0.81 were most similar to the EC measurements compared with the other two temporal scaling methods (see Figure 7 and Table 7). Relative to the vEFr method, the cEF method underestimated the total daytime ET. Because the EF curve is typically concave upward, the use of a constant EF value for an ASTER overpass underestimates the total daytime ET. The vEF method accounted for the spatial heterogeneity of the EF and minimized this disadvantage of the cEF method to some extent. However, the vEF method did not capture the EF fluctuation in the early morning or in the late afternoon, which affected the results of the vEF method relative to the vEFr method. The estimates from both the cEF and vEF methods have lower Corr. with the EC measurements than the vEFr method. The three methods underestimated the ET in areas with high f_c (see Tables 4–6), such as the fields of EC12, EC13 and EC14, compared with areas having low f_c . This difference is discussed in Section 5.4.

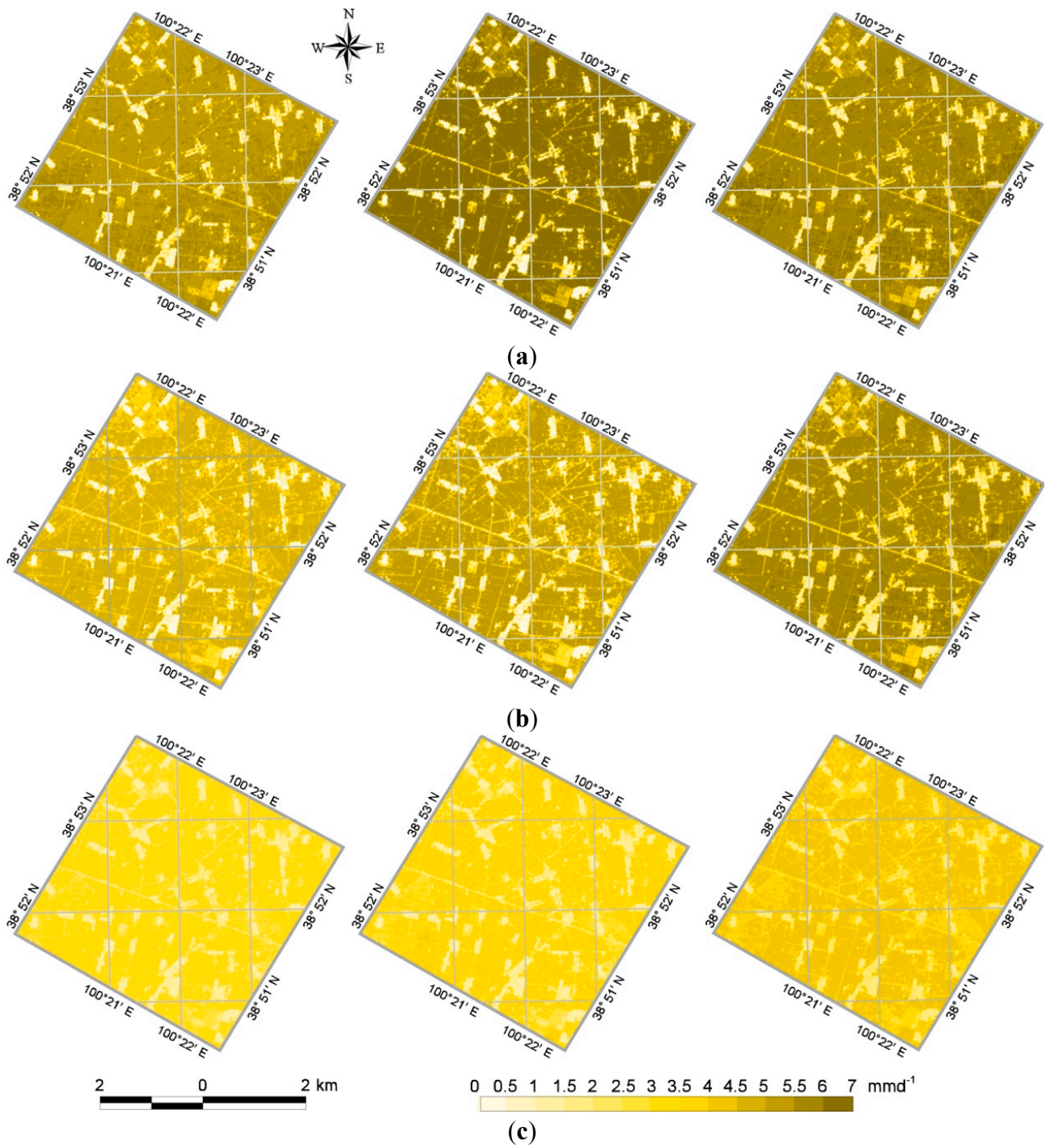


Figure 6. Maps of the total daytime ET (from 9:00 to 19:00) on (a) 10th July, (b) 2nd August and (c) 11th August of 2012 integrated using the cEF (left), vEF (middle) and vEFr (right) methods.

Table 4. Evapotranspiration (ET) validation on 10 July of 2012 (units: mm·d⁻¹).

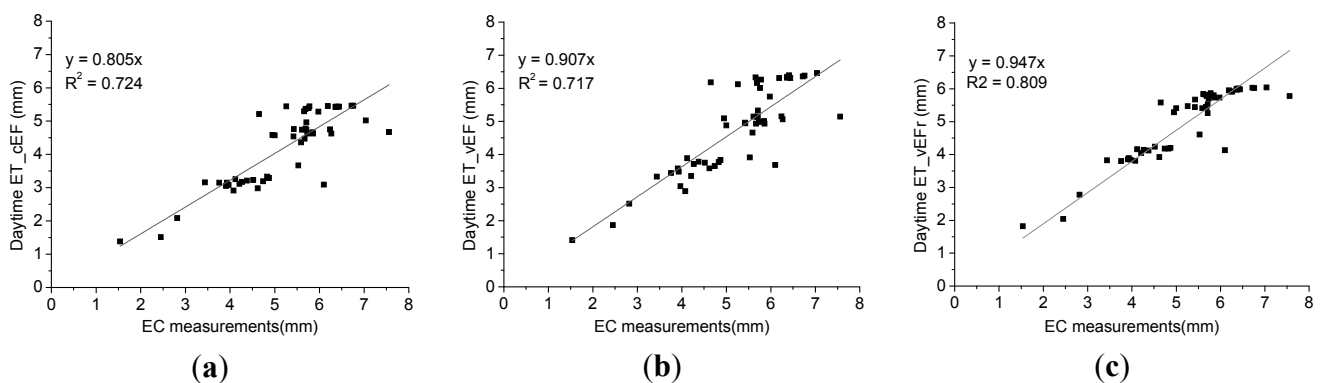
EC ID	f_c	EC	cEF	vEF	vEFr
EC01	0.8236	5.71	4.96	5.33	5.26
EC02	0.9278	5.76	5.39	6.01	5.79
EC03	0.9532	6.44	5.43	6.31	5.98
EC04	0.0000	2.82	2.08	2.51	2.78
EC05	0.9805	5.26	5.44	6.12	5.47
EC06	0.9916	6.37	5.43	6.35	5.97
EC07	0.9406	5.78	5.44	6.26	5.86
EC08	0.9732	6.72	5.46	6.36	6.03
EC09	0.9035	4.65	5.21	6.18	5.58
EC10	0.9935	6.19	5.45	6.31	5.95
EC11	0.9933	5.66	5.29	6.33	5.82
EC12	0.9922	6.41	5.43	6.39	6.01
EC13	1.0000	6.76	5.46	6.38	6.02
EC14	0.9905	7.04	5.02	6.46	6.04
EC15	0.9717	5.69	5.36	6.16	5.78
EC16	0.9839	6.36	5.42	6.32	6.00
EC17	0.8816	5.98	5.28	5.75	5.73

Table 5. ET validation on 2 August of 2012 (units: mm·d⁻¹).

EC ID	f_c	EC	cEF	vEF	vEFr
EC01	0.7836	5.53	3.67	3.91	4.61
EC02	0.9278	5.00	4.57	4.88	5.41
EC03	0.9532	5.86	4.62	4.93	5.73
EC04	0.0000	2.45	1.51	1.86	2.04
EC05	0.9805	4.95	4.58	5.09	5.28
EC06	0.9851	5.71	4.74	5.13	5.52
EC07	0.9406	5.73	4.62	4.98	5.70
EC08	0.9732	5.85	4.66	5.01	5.80
EC09	0.9035	5.42	4.54	4.96	5.44
EC10	0.9935	6.24	4.75	5.15	5.91
EC11	0.9933	5.43	4.76	4.94	5.67
EC12	0.9465	5.67	4.47	4.93	5.44
EC13	1.0000	5.61	4.74	5.14	5.84
EC14	0.9905	6.27	4.62	5.06	5.92
EC15	0.9717	5.69	4.77	5.14	5.45
EC16	0.9839	7.56	4.67	5.14	5.78
EC17	0.8816	5.59	4.36	4.66	5.41

Table 6. ET validation on 11 August of 2012 (units: mm·d⁻¹).

EC ID	f_c	EC	cEF	vEF	vEFr
EC01	0.8193	4.62	2.98	3.58	3.92
EC02	0.8604	4.21	3.11	3.35	4.04
EC03	0.8551	4.38	3.21	3.78	4.12
EC04	0.0000	1.54	1.38	1.41	1.82
EC05	0.8289	3.76	3.15	3.44	3.80
EC06	0.8677	3.93	3.15	3.48	3.89
EC07	0.8303	4.27	3.17	3.71	4.14
EC08	0.7912	3.91	3.05	3.58	3.85
EC09	0.8381	3.44	3.16	3.33	3.82
EC10	0.8747	4.52	3.23	3.75	4.24
EC11	0.7830	3.97	3.08	3.04	3.84
EC12	0.8320	4.74	3.19	3.65	4.18
EC13	0.8831	4.87	3.29	3.83	4.20
EC14	0.8734	4.83	3.33	3.77	4.18
EC15	0.8654	4.12	3.25	3.89	4.16
EC16	0.8556	6.10	3.09	3.68	4.13
EC17	0.7849	4.08	2.91	2.89	3.81

**Figure 7.** Comparison of the EC measurements and ET_{dt} based on the estimates from the (a) cEF, (b) vEF and (c) vEFr methods.**Table 7.** Validation statistics for the three ET temporal scaling methods.

	cEF	vEF	vEFr
RMSE (mm d ⁻¹)	1.19	0.85	0.54
MRE (%)	19.97	12.77	7.26
Corr.	0.72	0.72	0.81

5. Discussion

The variability or conservation of the EF on a given day is affected by a complex combination of factors, such as the weather, soil moisture, topography, biophysical conditions, cloud cover, moisture advection and heat advection. Thus, EF varies depending on various underlying surface and meteorological conditions. Four particular problems caused errors in the ET estimation during the temporal scaling process.

5.1. Spatial Heterogeneity of the EF

Two primary factors caused the spatial heterogeneity of the EF in our study area. First, the EF of farmlands differs from that of bare soil. The EF curves for regularly-irrigated farmlands are clearly concave upward, whereas those of bare soil during the daytime are more stable. The vEFr method uses Hoedjes's adjustment factor on farmlands under wet conditions when EF_t^{EC} is classified as stable. Second, particular abnormal meteorological and hydrological conditions in small areas or heterogeneous properties of the shallow subsurface also caused the spatial heterogeneity of the EF. The soil moisture conditions were not uniform because the fields could not all be irrigated simultaneously. Thus, the EF values were highly spatially heterogeneous when particular fields were irrigated but others were not. In our study, the midday EF value for each pixel used in the temporal scaling was calculated based on the remotely sensed EF_{ASTER} . However, the adjustment factor for the EF optimization and EF^{EC} for the temporal stability detection of the EF were calculated using *in situ* observations at the point scale. The second type of spatial heterogeneity was not considered in our study. The underestimation near tower EC03 on 10 July and 11 August represents a good example of this variation. These fields were irrigated two or three days before the ASTER overpass, *i.e.*, later than the irrigation of other fields; thus, their soil moisture was much higher than that of the other fields during the ASTER overpass. In addition, heterogeneous crop types can also lead to spatial heterogeneity in the EF. The underestimations near towers EC01, EC16 and EC17 are good examples of this variation. This spatial heterogeneity was addressed to an extent in this study. Only the first type of spatial heterogeneity was addressed using a dynamic coefficient that slightly adjusts the EF_{ASTER} value of farmlands. However, the second type of spatial heterogeneity requires extensive meteorological observations; the instruments required to make these observations are expensive. Thus, it was difficult to apply such methodology beyond the HiWATER context.

5.2. Temporal Heterogeneity of the EF

Solar radiation increases after 7:00 and decreases after 14:00; however, ET increases after 8:00 and decreases after 15:00 (see Figure 8). Thus, the EF produces a concave-upward curve with a linear decrease in the early morning and a sharp increase in the late afternoon, and the ET can be underestimated if a constant midday EF value during the satellite overpass is used in the temporal scaling process. The cEF method clearly underestimated the ET relative to the other two methods (see Table 7). The ETWatch model, which uses the cEF method for temporal scaling, has been shown to have a RMSE of 0.99 ($\text{mm}\cdot\text{d}^{-1}$) [37,47]. This problem was addressed by the vEF method to some extent, although the large fluctuations in the EF in the late afternoon were not identified with this method. If the temporal heterogeneity of the EF is not accounted for by temporal scaling, then the ET can be underestimated by 0.9 ($\text{mm}\cdot\text{d}^{-1}$) on a summer day. This amount is equivalent to approximately 16% of the total daytime ET in farmland in arid regions on a summer day. Using our detection algorithm for the temporal stability of the EF, the ET temporal scaling method yielded more accurate values (30 m resolution), with an RMSE of 0.54 ($\text{mm}\cdot\text{d}^{-1}$), MRE of 7.26% and Corr. of 0.81, which are improvements over the other two methods.

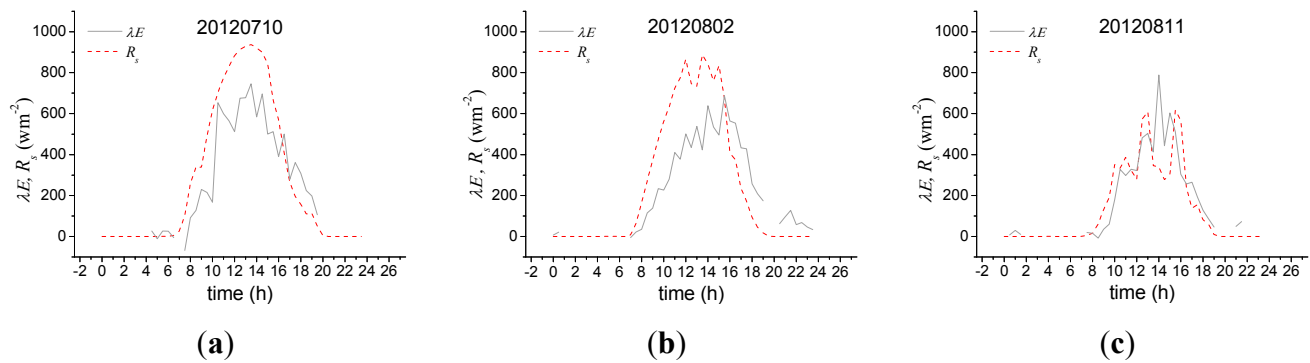


Figure 8. Comparison of λE from observations of tower EC12 and the total solar radiation from AMS12 on (a) 10 July, (b) 2 August and (c) 11 August of 2012.

EF^{EC} should represent the properties of the EF across most of the area because the spatial heterogeneity caused by particularly abnormal small-scale meteorological and hydrological states was not considered. Thus, the ET should be estimated several days after irrigation, when the soil moisture becomes homogeneous across the area.

5.3. The Uncertainty in Input

Instrumentation errors and the estimation errors for the instantaneous surface heat fluxes were analyzed in this study. The uncertainty in the EC measurements was approximately 16% [48]. The observation error of the net radiation (CNR 1) was approximately 20 ($\text{W}\cdot\text{m}^{-2}$) [49]. These errors were considered when calculating the EF^{EC} values that were used as reference EF values in the detection algorithm for the temporal stability of the EF. The remotely sensed instantaneous R_n , G and λE values had errors of 2–3 ($\text{W}\cdot\text{m}^{-2}$), 9–12 ($\text{W}\cdot\text{m}^{-2}$), and 7–11 ($\text{W}\cdot\text{m}^{-2}$), respectively [35]. These errors were considered in the calculation of EF_{ASTER} and β_{ASTER} , which were used as the midday constant EF value and the determination index for wet conditions, respectively.

5.4. The Saturation of f_c

f_c is another factor that affects the ET estimates. After July, seed corn in the Zhangye Oasis usually reaches 1.6 m in height. The crop leaves are large and overlapping, and the field ridges are closely spaced. Transpiration significantly contributes to the total ET at this time, and the percentage of transpiration to the total ET reaches $85.69\% \pm 5.86\%$ [50]. According to the equation for f_c (Equation (12)) [42], when an NDVI value surpasses the maximum value, f_c becomes 100%. However, when f_c becomes saturated (close to 100%), the LAI continues to increase (see Figure 9). f_c cannot account for the effects of stacked leaves. Moreover, f_c was not only used in the estimation of the instantaneous emissivity [41,42], G [9], and λE [35] at the ASTER overpasses but also used in the derivation of the LST . This saturation effect of f_c on the ET estimation requires further analysis. The ET should be underestimated in densely planted farmlands, where as EF_{ASTER} should be underestimated during an ASTER overpass based on these errors. Consequently, the three methods underestimated the ET in the fields with high f_c , particularly in the fields near towers EC06, EC12, EC13 and EC14. The ET is underestimated by $0.3 (\text{mm}\cdot\text{d}^{-1})$ when f_c is nearly 100%.

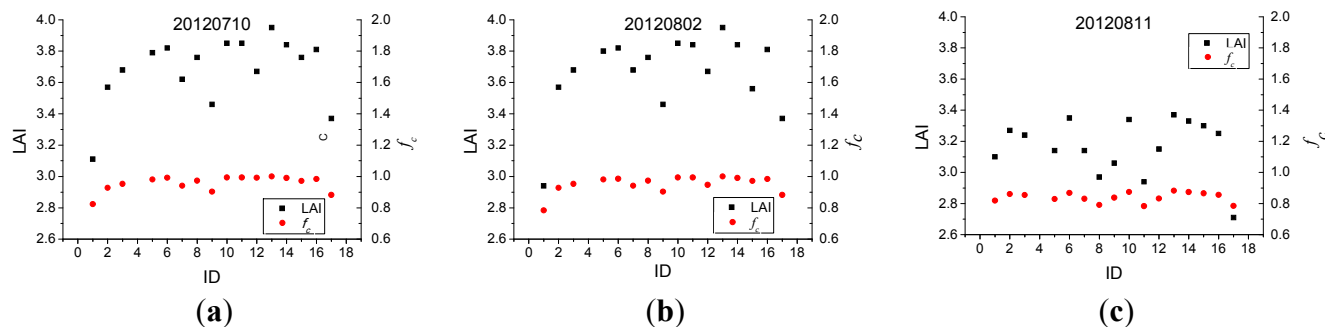


Figure 9. Comparison of the LAI and f_c at 17 AMS/EC stations on (a) 10 July, (b) 2 August and (c) 11 August of 2012.

5.5. The Transferability and Limitations of vEFr

Humidity, four radiation components, LST, and half-hourly λE and G are required for the vEFr method. According to the input data of the vEFr method, one ordinary AMS and one automatic infrared thermometer are required to use the vEFr method in other areas. If conditions permit, it is more preferable to utilize one or more EC systems. The reason is that the eddy covariance method [51] is regarded as the most reliable method for calculating half-hourly λE values [48], which are used to calculate the reference EF^{EC} values used in the detection algorithm for the temporal stability of the EF and to validate the final ET estimate. If the EC system is unavailable under limited conditions, the vertical gradient method [52] using two layers of AMS observations is an alternative to the eddy covariance method [51] for calculating half-hourly λE values and the total daytime ET.

The vEFr method has two limitations in application. First, the orographic effect was not considered in the vEFr method, so the impacts of advection, changing wind and humidity conditions could not be captured in ET temporal scaling. Thus, the vEFr method should be applied in flat farmlands. Second, the EF^{EC} values that were used as reference EF values in the detection algorithm for the temporal stability of the EF was a point observation, so spatial heterogeneity in EF caused by heterogeneous soil moisture conditions and crop types would bring about larger errors in estimation. Thus, the vEFr method was more applicable for regularly-irrigated farmlands with relatively homogeneous crops at the regional scale. In addition, due to the second limitation of the vEFr method, remotely sensed images with a spatial resolution of about 30 m (*i.e.*, Landsat 8 OLI/TIRS image) were more preferable to implement the vEFr method.

6. Conclusions

In regularly-irrigated farmland, the instability of the EF in the afternoon is the main cause of the ET underestimation by the cEF and vEF temporal scaling methods. The revised vEFr temporal scaling method yielded better ET estimates because it considers the temporal heterogeneity of the EF in the afternoon. The vEFr method easily extends to other areas and exhibits a superior performance in flat and regularly-irrigated farmlands at the regional scale.

Acknowledgements

This work was supported by the Knowledge Innovation Program of the Chinese Academy of Sciences (grant KZCX2-EW-312) and by the National Natural Science Foundation of China (grants 41201372, 41301362 and 41401412). The editors and reviewers generously helped revise the paper.

Author Contributions

Yi Song and Long Jin designed the case study. Mingguo Ma and Xufeng Wang processed the data. Yi Song analyzed the data and wrote the paper. All of the authors contributed to the discussion of the results.

Conflicts of Interest

The authors declare no conflict of interest.

References

1. Bastiaanssen, W.G.M.; Molden, D.J.; Makin, I.W. Remote sensing for irrigated agriculture: Examples from research and possible applications. *Agric. Water Manag.* **2000**, *46*, 137–155.
2. Su, Z. Remote sensing of land use and vegetation for mesoscale hydrological studies. *Int. J. Remote Sens.* **2000**, *21*, 213–233.
3. Li, Z.; Tang, R.; Wan, Z.; Bi, Y.; Zhou, C.; Tang, B.; Yan, G.; Zhang, X. A review of current methodologies for regional evapotranspiration estimation from remotely sensed data. *Sensors* **2009**, *9*, 3801–3853.
4. Allen, R.G. Using the FAO-56 dual crop coefficient method over an irrigated region as part of an evapotranspiration intercomparison study. *J. Hydrol.* **2000**, *229*, 27–41.
5. Porporato, A.; Daly, E.; Rodriguez-Iturbe, I. Soil water balance and ecosystem response to climate change. *Am. Nat.* **2004**, *164*, 625–632.
6. Myneni, R.B.; Hoffman, S.; Knyazikhin, Y.; Privette, J.L.; Glassy, J.; Tian, Y.; Wang, Y.; Song, X.; Zhang, Y.; Smith, G.R.; *et al.* Global products of vegetation leaf area and fraction absorbed PAR from year one of MODIS data. *Remote Sens. Environ.* **2002**, *83*, 214–231.
7. Huete A.; Didan, K.; Miura, T.; Rodriguez, E.P.; Gao, X.; Ferreira, L.G. Overview of the radiometric and biophysical performance of the MODIS vegetation indices. *Remote Sens. Environ.* **2002**, *83*, 195–213.
8. Chen, Y.; Xia, J.; Liang, S.; Feng, J.; Fisher, J.B.; Li, X.; Li, X.L.; Liu, S.; Ma, Z.; Miyata, A.; *et al.* Comparison of satellite-based evapotranspiration models over terrestrial ecosystems in China. *Remote Sens. Environ.* **2014**, *140*, 279–293.
9. Su, Z. The Surface Energy Balance System (SEBS) for estimation of turbulent heat fluxes. *Hydrol. Earth Syst. Sci.* **2002**, *6*, 85–99.
10. Bastiaanssen, W.G.M.; Menenti, M.; Feddes, R.A.; Holtslag, A.A. A remote sensing surface energy balance algorithm for land (SEBAL): I. Formulation. *J. Hydrol.* **1998**, *212–213*, 198–212.
11. Long, D.; Singh, V.P. A two-source trapezoid model for evapotranspiration (TTME) from satellite imagery. *Remote Sens. Environ.* **2012**, *121*, 370–388.

12. Xin, X.; Liu, Q. The Two-layer Surface Energy Balance Parameterization Scheme (TSEBPS) for estimation of land surface heat fluxes. *Hydrol. Earth Syst. Sci.* **2010**, *14*, 491–504.
13. Jackson, R.D.; Hatfield, J.L.; Reginato, R.J.; Idso, S.B.; Pinter, P.J. Estimation of daily evapotranspiration from one time of day measurements. *Agric. Water Manag.* **1983**, *7*, 351–362.
14. Sugita, M.; Brutsaert, W. Daily evaporation over a region from lower boundary layer profiles measured with radiosondes. *Water Resour. Res.* **1991**, *27*, 747–752.
15. Zhang, L.; Lemeur, R. Evaluation of daily evapotranspiration estimates from instantaneous measurements. *Agric. For. Meteorol.* **1995**, *74*, 139–154.
16. Allen, R.G.; Tasumi, M.; Trezza, R. Satellite-based energy balance for mapping evapotranspiration with internalized calibration (METRIC)-model. *J. Irrig. Drain. Eng.* **2007**, *133*, 380–394.
17. Tomás, A.; Nieto, H.; Guzinski, R.; Salas, J.; Sandholt, I.; Berliner, P. Validation and scale dependencies of the triangle method for the evaporative fraction estimation over heterogeneous areas. *Remote Sens. Environ.* **2014**, *152*, 493–511.
18. Crago, R.D. Conservation and variability of the evaporative fraction during the daytime. *J. Hydrol.* **1996**, *180*, 173–194.
19. Hoedjes, J.C.B.; Chehbouni, A.; Jacob, F.; Ezzahar, J.; Boulet, G. Deriving daily evapotranspiration from remotely sensed instantaneous evaporative fraction over olive orchard in semi-arid Morocco. *J. Hydrol.* **2008**, *354*, 53–64.
20. Gentine, P.; Entekhabi, D.; Chehbouni, A.; Boulet, G.; Duchemin, B. Analysis of evaporative fraction diurnal behavior. *Agric. For. Meteorol.* **2007**, *143*, 13–29.
21. Gentine, P.; Entekhabi, D.; Polcher, J. The diurnal behavior of evaporative fraction in the soil-vegetation-atmospheric boundary layer continuum. *J. Hydrometeorol.* **2011**, *12*, 1530–1546.
22. Lu, J.; Tang, R.; Tang, H.; Li, Z. Derivation of daily evaporative fraction based on temporal variations in surface temperature, air temperature, and net radiation. *Remote Sens.* **2013**, *5*, 5369–5396.
23. Suleiman, A.; Crago, R.D. Hourly and daytime evapotranspiration from grassland using radiometric surface temperatures. *Agron. J.* **2004**, *96*, 384–390.
24. Cheng, G.; Li, X.; Zhao, W.; Xu, Z.; Feng, Q.; Xiao, S.; Xiao, H. Integrated study of the water-ecosystem-economy in the Heihe River Basin. *Natl. Sci. Rev.* **2014**, *1*, 413–428.
25. Yang, D.; Chen, H.; Lei, M. Analysis of the diurnal pattern of evaporative fraction and its controlling factors over croplands in the Northern China. *J. Integr. Agric.* **2013**, *12*, 1316–1329.
26. Li, X.; Cheng, G.; Liu, S.; Xiao, Q.; Ma, M.; Jin, R.; Che, T.; Liu, Q.; Wang, W.; Qi, Y.; *et al.* Heihe Watershed Allied Telemetry Experimental Research (HiWATER): Scientific objectives and experimental design. *Bull. Am. Meteorol. Soc.* **2013**, *94*, 1145–1160.
27. Xu, Z.; Liu, S.; Li, X.; Shi, S.; Wang, J.; Zhu, Z.; Xu, T.; Wang, W.; Ma, M. Intercomparison of surface energy flux measurement systems used during the HiWATER-MUSOEXE. *J. Geophys. Res.* **2013**, *118*, 13140–13157.
28. Vickers, D.; Mahrt, L. Quality control and flux sampling problems for tower and aircraft data. *J. Atmos. Ocean. Technol.* **1997**, *14*, 512–526.
29. Wilczak, J.M.; Oncley, S.P.; Stage, S.A. Sonic anemometer tilt correction algorithms. *Bound.-Layer Meteorol.* **2001**, *99*, 127–150.

30. Schotanus, P.; Nieuwstadt, F.T.M.; DeBruin, H.A.R. Temperature measurement with a sonic anemometer and its application to heat and moisture fluctuations. *Bound.-Layer Meteorol.* **1983**, *26*, 81–93.
31. Moore, C.J. Frequency response corrections for eddy correlation systems. *Bound.-Layer Meteorol.* **1986**, *37*, 17–35.
32. Webb, E.K.; Pearman, G.I.; Leuning, R. Correction of the flux measurements for density effects due to heat and water vapour transfer. *Q. J. R. Meteorol. Soc.* **1980**, *106*, 85–100.
33. Liu, S.; Xu, Z.; Wang, W.; Bai, J.; Jia, Z.; Zhu, M.; Wang, J. A comparison of eddy-covariance and large aperture scintillometer measurements with respect to the energy balance closure problem. *Hydrol. Earth Syst. Sci.* **2011**, *15*, 1291–1306.
34. Colaizzi, P.D.; Evett, S.R.; Howell, T.A.; Tolck, J.A. Comparison of five models to scale daily evapotranspiration from one-time-of-day measurements. *Trans. ASAE* **2006**, *49*, 1409–1417.
35. Song, Y.; Wang, J.; Yang, K.; Ma, M.; Li, X.; Zhang, Z.; Wang, X. A revised surface resistance parameterisation for estimating latent heat flux from remotely sensed data. *Int. J. Appl. Earth Obs. Geoinf.* **2012**, *17*, 76–84.
36. Yang, K.; Wang, J. A temperature prediction–correction method for estimating surface soil heat flux from soil temperature and moisture data. *Sci. China Series D: Earth Sci.* **2008**, *51*, 721–729.
37. Jia, Z.; Liu, S.; Xu, Z.; Chen, Y.; Zhu, M. Validation of remotely sensed evapotranspiration over the Hai River Basin, China. *J. Geophys. Res.* **2012**, *117*, doi:10.1029/2011JD01703.
38. Kormann, R.; Meixner, F. An analytical footprint model for non-neutral stratification. *Bound.-Layer Meteorol.* **2001**, *99*, 207–224.
39. Jacob, F.; Oliosio, A. Derivation of diurnal courses of albedo and reflected solar irradiance from airborne POLDER data acquired near solar noon. *J. Geophys. Res.* **2005**, *110*, doi:10.1029/2004JD00488.
40. Liang, S. Narrowband to broadband conversions of land surface albedo: I Algorithms. *Remote Sens. Environ.* **2001**, *76*, 213–238.
41. Sobrino, J.A.; Jimenez-Munoz, J.C.; Soria, G.; Romaguera, M.; Guanter, L.; Moreno, J.; Plaza, A.; Martinez, P. Land surface emissivity retrieval from different VNIR and TIR sensors. *IEEE Trans. Geosci. Remote Sens.* **2008**, *46*, 316–327.
42. Qin, Z.; Karnieli, A. A mono-window algorithm for retrieving land surface temperature from Landsat TM data and its application to the Israel-Egypt border region. *Int. J. Remote Sens.* **2001**, *22*, 3719–3746.
43. Carlson, T.N.; Ripley, D.A. On the relation between NDVI, fractional vegetation cover and leaf area index. *Remote Sens. Environ.* **1997**, *62*, 241–252.
44. Wan, Z.; Zhang, Y.; Zhang Q.; Li, Z. Validation of the landsurface temperature products retrieved from Terra Moderate Resolution Imaging Spectroradiometer data. *Remote Sens. Environ.* **2002**, *83*, 163–180.
45. Monteith, J.L. *Principles of Environmental Physics*; Edward Arnold: London, UK, 1973; p. 241.
46. Kustas, W.P.; Daughtry, C.S.T. Estimation of the soil heat flux/net radiation ratio from spectral data. *Agric. For. Meteorol.* **1989**, *49*, 205–223.

47. Wu, B.; Yan, N.; Xiong, J.; Bastiaanssen, W.G.M.; Zhu, W.; Stein, A. Validation of ETWatch using field measurements at diverse landscapes: A case study in Hai Basin of China. *J. Hydrometeorol.* **2012**, *436–437*, 67–80.
48. Wang, J.; Zhuang, J.; Wang, W.; Liu, S.; Xu, Z. Assessment of uncertainties in eddy covariance flux measurement based on intensive flux matrix of HiWATER-MUSOEXE. *IEEE Geosci. Remote Sens. Lett.* **2014**, *12*, 259–263.
49. Kohsiek, W.; Liebenthal, C.; Foken, T.; Vogt, R.; Oncley, S.P.; Bernhofer, C.; Debruin H.A.R. The energy balance experiment EBEX-2000. Part III: Behaviour and quality of the radiation measurements. *Bound.-Layer Meteorol.* **2007**, *123*, 55–75.
50. Wen, X.; Lee, X.; Sun, X.; Wang, J.; Hu, Z.; Li, S.; Yu, G. Dew water isotopic ratios and their relations to ecosystem water pools and fluxes in a cropland and a grassland in China. *Oecologia.* **2012**, *168*, 549–561.
51. Swinbank, W.C. Measurement of vertical transfer of heat and water vapour by eddies in the low atmosphere. *J. Meteorol.* **1951**, *8*, 135–145.
52. Thornthwait, C.W.; Holzman, A. Report of the commutation on transpiration and evaporation. *Trans. Am. Geophys. Union* **1944**, *25*, 683–693.

© 2015 by the authors; licensee MDPI, Basel, Switzerland. This article is an open access article distributed under the terms and conditions of the Creative Commons Attribution license (<http://creativecommons.org/licenses/by/4.0/>).